Prediction of long-term extreme load effects due to wind for cable-supported bridges using time-domain simulations*

Yuwang Xu[a], Ole Øiseth[a], Arvid Naess[b], Torgeir Moan[c]

a Department of Structural Engineering, Norwegian University of Science and Technology, Richard Birkelands vei 1, Norway

b Department of Mathematical Sciences, Norwegian University of Science and Technology, Alfred Getz vei 1, Norway

c Department of Marine Technology, Norwegian University of Science and Technology, O. Nielsens v 10, Norway

Abstract

Many long-span bridges that are slender and susceptible to wind-induced vibrations are currently under construction all over the world. As nonlinear structural behavior and nonlinear displacement-dependent wind loads become of higher importance, time-domain methods are commonly applied instead of frequency-domain approaches. This paper discusses how rational functions, fitted to aerodynamic derivatives, can be converted to a state-space model to transform the frequency-dependent aerodynamic forces into the time domain. A user element has been implemented in ABAQUS to include the self-excited forces in the dynamic analysis. The flutter stability limit and buffeting response of the Hardanger Bridge have been calculated in a comprehensive case study to illustrate the performance of the presented methodology. The Average Conditional Exceedance Rate method is used to estimate long-term extreme load effects. A simplified full long-term method that ignores wind velocities which contribute little to the long-term extreme values is introduced to reduce the required computational effort. The long-term predictions are also compared with results obtained using a short-term approach and it is concluded that the long-term extreme load effects are approximately 20% higher than the short-term extreme values.

Keywords:

Self-excited wind forces, time domain, state-space method, long-term extreme value analysis

* *Corresponding author: Ole Øiseth. Tel.: +4773591493; E-mail address: ole.oiseth@ntnu.no*
Published in Engineering Structures
DOI: 10.1016/j.engstruct.2017.06.051

1. Introduction

Flutter and dynamic behavior in strong winds are always two of the main concerns when designing long-span bridges. The self-excited forces cause flutter, while both the self-excited and the buffeting forces are important for the dynamic response of bridges in strong winds. The multi-mode frequency-domain method has been widely used to study flutter stability and dynamic response to strong winds [1-3]. The method will provide results of high accuracy if there are no strong nonlinear characteristics in the system. Modern bridge designs, however, are characterized by high flexibility and sensitivity to wind actions due to the increased span lengths. As a consequence, time-domain modelling of the self-excited forces has received much attention in recent years [3-15]. One possibility is to use quasi-steady theory by modelling the self-excited forces using coefficients from static wind tunnel tests. The coefficients in the model are frequency-independent, making the model convenient to implement in the time domain. Diana et al. [8] developed a corrected quasi-steady theory by including aerodynamic nonlinearities. The predicted quasi-steady aerodynamic forces were reasonable but not perfectly correct. The low reduced velocity range is particularly hard to capture accurately. The fluid memory effect can be taken into account not only by transfer functions in the frequency domain but also by convolution integrals in the time domain. Scanlan et al. [16, 17] generalized the Wagner function that was originally developed for airplane wings and applied it for bridge decks to represent the self-excited forces. The Wagner function is also addressed as an indicial function and has been widely used by many research studies in time-domain simulation of unsteady self-excited aerodynamic forces [5, 6, 13, 18]. The challenge is to fit the various models to the experimental data of the aerodynamic derivatives. The most common approach thus far is to approximate the aerodynamic derivatives using rational functions, which is also known as Roger's approximation [19].

Most of the studies mentioned above were limited to simple systems, such as a two-degrees-of-freedom section model. In bridge design, it is necessary to include self-excited forces in a finite element analysis of the entire bridge. Borri et al. [18] and Salvatori and Spinelli [13] expressed the self-excited forces in the time domain by indicial functions. Borri et al. [18] checked the time domain load model with a three-dimensional full-bridge model in the finite element code FEMAS. Salvatori

and Spinelli [13] developed a finite element program capable of handling simplified bridge models and found that the structural nonlinearities could limit the oscillation amplitudes in super-critical velocity range and deemphasize the presence of the critical wind velocity. Chen et al. [5, 6] and Arena et al. [20] replaced the convolution integrals with a state-space model, making the numerical simulation more efficient. Chen et al. [5, 6] conducted the flutter and buffeting analysis in the time domain, but in terms of generalized modal coordinates. Their studies showed that the response increased slightly when the nonlinear unsteady aerodynamic forces are considered. Arena et al. [20] analyzed the flutter and the dynamic response of long-span suspension bridge considering nonuniform span-wise wind profile and time- and space-dependent gust loading conditions, respectively. The dynamic behavior was found significantly different from that under uniform gust loading conditions. Øiseth et al. [12] also used a state-space model and introduced the state variables as additional degrees of freedom in each node of a beam element to simulate the fluid memory effect. The critical velocity and the buffeting response predicted by the model corresponded well to the frequency-domain results. It is, however, a significant drawback that it is rather complicated to introduce additional degrees of freedom into existing finite element programs.

It is the extreme deflections and load effects that are relevant for design. Long-term analysis is the most accurate approach to obtain the N-year load effects for ultimate limit state (ULS) design checks. Nevertheless, short-term analyses are still widely used because the long-term approach normally requires massive computational effort, especially when it is necessary to consider the variability of, for instance, the mean wind velocity, wind direction, turbulence intensities and integral length scales by means of a joint probability distribution. In short-term analysis, the N-year load effects are approximated by the extreme values for a short-term environmental condition with a selected return period and duration, for instance, 100 years and 10 minutes. The design load effect obtained from the short-term analysis needs to be multiplied by a factor to take into account the fact that less severe conditions that occur more frequently and more severe conditions that occur less frequently will also contribute to the long-term extreme value distribution. This approach generally needs to be verified by a full long-term analysis. Many studies of short- and long-term extreme load effects for marine structures have been conducted over the years [21-24].

The Gumbel method [25, 26] and the Weibull tail method [21, 27] are widely used for short-term extreme value analysis. In the Gumbel method, the single largest maximum value is extracted from each simulation, and the sample of the independent maxima from an ensemble of simulations is assumed to follow the Gumbel distribution. In the Weibull tail method, all peaks above a selected threshold are extracted, and the tail regime is fitted to a Weibull distribution. The empirically selected threshold is very important for the predicted results, which can be a disadvantage. Naess and Gaidai [28] developed an Average Conditional Exceedance Rate (ACER) method to estimate the extreme values from sampled short-term time series, which can account for the dependence of the neighboring up-crossings. This method has been widely used for many applications [23, 24, 29]. Saha compared the predicted short-term extreme response of an offshore wind turbine subjected to wind and wave loading with applications of the up-crossing rate method, Gumbel method and Weibull tail method. The up-crossing rate method performed better in his case.

For estimation of long-term extreme value distributions, the full long-term method, which is the convolution of short-term distributions for all environmental conditions, is the most accurate but requires massive computational effort. More efficient approximate methods have been introduced over the years. For areas governed by occurrences of some extreme storms, the “peaks over threshold” approach is recommended [30, 31]. It is more effective than the classical approach because it only considers the exceedance probabilities from a limited number of environment events, e.g., severe storms or hurricanes. The environmental contour method is discussed in [32, 33], in which only one single short-term environmental condition with the desired return period is required to obtain the extreme value distribution. This method is widely used in offshore engineering. Li introduced a modified environmental contour method in bottom-fixed offshore wind turbines to take into account the non-monotonic behavior of the response under wind loads. He also applied a simplified full long-term method, which considers only the environmental conditions that give significant contributions to the long-term extreme values.

Although many studies of long-term extreme value analysis have been carried out for marine structures, very few studies of wind-induced load effects for civil engineering structures seem to exist. Some studies have been conducted for high-rise buildings [34, 35], but the authors have not found any

contributions related to long-term analysis of cable-supported bridges. Both time- and frequency-domain methods can be applied to carry out the long-term extreme value analysis. The analysis will be carried out in the time domain in this paper because it is convenient to include non-liner behavior in the analysis. A full long-term method is very computationally demanding, making efficient simulations essential. The self-excited forces are therefore modelled by applying a state-space model. The state variables are solved directly at the element level and considered in the analysis by developing a finite element, making it unnecessary to include them in the global system matrices. A full long-term analysis of important load effects has been studied in detail, and a possible approximation considering only mean wind velocities that contribute significantly to the long-term extreme value distributions has been investigated. A short-term analysis has also been carried out to investigate how short-term extremes can be used to approximate the long-term extreme values.

2. Wind-induced dynamic response

The equation of motion for a cable-supported bridge subjected to wind loading is

$$\mathbf{M}\ddot{\mathbf{u}}(\mathrm{t}) + \mathbf{C}\dot{\mathbf{u}}(t) + \mathbf{K}\mathbf{u}(t) = \mathbf{F}_{wind}(\mathrm{t})\,. \tag{1}$$

Here, **M**, **C** and **K** symbolize the still-air mass, damping and stiffness matrix, respectively; **u** represents the degrees of freedom of the finite element model. $\mathbf{F}_{wind}$ represents the wind actions that consist of a time invariant part due to the mean wind velocity, and a dynamic part due to turbulence in the wind field, vortex shedding and self-excited forces generated by the motion of the structure. Since vortex shedding induced vibrations typically occur at very low mean wind velocities and will usually not give a significant contribution to the long-term extreme value distribution of the load effects, this paper will focus on modelling of wind loading due to the mean wind velocity, turbulence and the motion of the structure. A special attention is put into how one can model the self-excited forces in an efficient manner to reduce the required computational effort.

2.1 Efficient modelling of self-excited forces

2.1.1 Simulation of self-excited wind force in the time domain

The self-excited forces acting on a bridge deck section are commonly represented by the aerodynamic derivatives developed by Scanlan and Tomo [16]. The self-excited forces **q** for a bridge deck in a single-frequency harmonic motion can be expressed as follows

$$\mathbf{q} = \mathbf{C}_{ae}(K)\dot{\mathbf{u}} + \mathbf{K}_{ae}(K)\mathbf{u} \,. \tag{2}$$

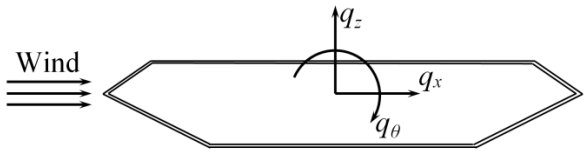

Fig. 1 Aerodynamic forces acting on a cross-section of a bridge deck

Here, $\mathbf{q} = [q_x \; q_z \; q_\theta]^T$ and $\mathbf{u} = [u_x \; u_z \; u_\theta]^T$ represent the self-excited forces and displacements of a single-frequency harmonic motion, respectively. The forces and moment in the positive directions are shown in Fig. 1. The displacements are positive in the same direction as the forces. *K* is reduced frequency $K = (B\omega)/V$ and ω refers to the oscillation frequency of the bridge deck. The aerodynamic damping matrix, $\mathbf{C}_{ae}$, and the aerodynamic stiffness matrix, $\mathbf{K}_{ae}$, which contain 18 aerodynamic derivatives, P_n^*, H_n^* and A_n^*, $n \in \{1,2,...,6\}$, can be written as

$$\mathbf{C}_{ae} = \frac{1}{2}\rho VKB\begin{bmatrix} P_1^* & P_5^* & BP_2^* \\ H_5^* & H_1^* & BH_2^* \\ BA_5^* & BA_1^* & B^2A_2^* \end{bmatrix}, \; \mathbf{K}_{ae} = \frac{1}{2}\rho V^2K^2\begin{bmatrix} P_4^* & P_6^* & BP_3^* \\ H_6^* & H_4^* & BH_3^* \\ BA_6^* & BA_4^* & B^2A_3^* \end{bmatrix}.$$

Here, *V* denotes the mean wind velocity, ρ represents the air density, and *B* symbolizes the width of the girder. Eq. (2) is only valid for a single-frequency harmonic motion. By introducing the principle of superposition, the model can be extended to any period or aperiodic motion through Fourier integral representation

$$\begin{aligned} \mathbf{G}_q(\omega) &= (i\omega\mathbf{C}_{ae}(\omega) + \mathbf{K}_{ae}(\omega))\mathbf{G}_u(\omega) \\ &= \mathbf{F}(\omega)\mathbf{G}_u(\omega) \end{aligned} \,. \tag{3}$$

Here, $\mathbf{G}_q(\omega)$ and $\mathbf{G}_u(\omega)$ represent the self-excited forces and displacements of any period or aperiodic motion in the frequency domain. Applying the inverse Fourier transform to Eq. (3), the self-excited force can be expressed in the time domain as follows

$$\mathbf{q}(\mathrm{t}) = \int_{-\infty}^{\infty} \mathbf{f}(\mathrm{t}-\tau)\mathbf{u}(\tau)d\tau \ . \tag{4}$$

Here, **f**(t) and **u**(t) are the inverse Fourier transforms of $\mathbf{F}(\omega)$ and $\mathbf{G}_u(\omega)$.

The aerodynamic derivatives are commonly known only at discrete reduced frequencies, and hence a continuous expression needs to be curve-fitted to experimental data to perform the integration over the range of (-∞,∞). To develop a time-domain representation of self-excited forces, the selected expression must be suitable for inverse Fourier transformation. The following rational function expression has been frequently used in the literature [5, 6, 11, 12]

$$\mathbf{F}(\omega) = \frac{1}{2}\rho V^2 (\mathbf{a}_1 + \mathbf{a}_2 \frac{i\omega B}{V} + \sum_{l=1}^{N-3} \mathbf{a}_{l+3} \frac{i\omega B/V}{i\omega B/V + d_l}) \ . \tag{5}$$

The unknowns $\mathbf{a}_1$, $\mathbf{a}_2$, $\mathbf{a}_{l+3}$ and d_l are obtained by applying a least squares fit to the experimental data of the aerodynamic derivatives, which are usually obtained through wind tunnel experiments. Taking the inverse Fourier transform of Eq. (5) and inserting the result into Eq. (4) gives the following expression for the self-excited forces (see [12] for further details)

$$\mathbf{q}(\mathrm{t}) = \frac{1}{2}\rho V^2 (\mathbf{a}_1 \mathbf{u}(\mathrm{t}) + \frac{B}{V}\mathbf{a}_2 \dot{\mathbf{u}}(\mathrm{t}) + \sum_{l=1}^{N-3} \mathbf{a}_{l+3} (\mathbf{u}(\mathrm{t}) - \frac{d_l V}{B} \int_{-\infty}^{t} e^{-(d_l V/B)(\mathrm{t}-\tau)} \mathbf{u}(\mathrm{t}) d\tau)) \ . \tag{6}$$

If we consider $\mathbf{q}(y,t)$ as a distributed load acting on a beam element, it has to be transformed to the self-excited nodal force $\mathbf{F}_{se}(\mathrm{t})$. The displacement along the girder $\mathbf{u}(y,\mathrm{t})$ can be expressed as

$$\mathbf{u}(y,t) = \mathbf{N}(y)\mathbf{v}(\mathrm{t}) \ . \tag{7}$$

Here, the matrix $\mathbf{N}(y)$ includes the shape functions and the vector **v**(t) contains the nodal displacement degrees of freedom. Based on the principle of virtual work,

$$\mathbf{F}_{se}(\mathrm{t}) = \int_0^l \mathbf{N}^T(y)\mathbf{q}(y,\mathrm{t})dy \ . \tag{8}$$

Here l refers to the length of the beam element. Substituting Eqs.(6) and (7) to the equation above, the self-excited nodal force can be expressed as follows, see [12] for further details

$$\begin{cases} \mathbf{F}_{se} = \mathbf{A}_1\mathbf{v}(\mathrm{t}) + \mathbf{A}_2\dot{\mathbf{v}}(\mathrm{t}) + \mathbf{Z}(\mathrm{t}) \\ \mathbf{Z}(\mathrm{t}) = \mathbf{Q}\mathbf{X}(\mathrm{t}) \end{cases}, \tag{9}$$

where

$$\mathbf{A}_1 = \frac{1}{2}\rho V^2 \int_0^l \mathbf{N}^T(y)\mathbf{a}_1\mathbf{N}(y)dy; \qquad \mathbf{A}_2 = \frac{1}{2}\rho V^2 \frac{B}{V}\int_0^l \mathbf{N}^T(y)\mathbf{a}_2\mathbf{N}(y)dy;$$
$$\mathbf{Q} = [\mathbf{A}_4\ \mathbf{A}_5 \cdots \mathbf{A}_N]; \qquad \mathbf{X} = [\mathbf{x}_1\ \mathbf{x}_2 \cdots \mathbf{x}_{N-3}]^T.$$

Here, $\mathbf{A}_{l+3} = \frac{1}{2}\rho V^2 \int_0^l \mathbf{N}^T(y)\mathbf{a}_{l+3}\mathbf{N}(y)dy$ and $\mathbf{x}_l = \mathbf{v}(\mathrm{t}) - \frac{d_l V}{B}\int_{-\infty}^t e^{-(d_l V/B)(\mathrm{t}-\tau)}\mathbf{v}(\tau)\,\mathrm{d}\tau$.

2.1.2 State-space modelling of the self-excited forces

Efficient modelling of the self-excited forces is of crucial importance because many time series need to be obtained to assess the long-term extremes distributions of the load effects. Several approaches have been presented in the literature. Chen [5, 6], Salvatori [13] and Borri [18] expressed the self-excited force in the time domain by indicial functions, and implemented the theory for three-dimensional full-bridges. Salvatori and Spinelli [13] and Borri et al. [18] dealt with the time-history-dependent part of the self-excited force via convolution integrals, which are calculated and updated at each time step. As noted by several authors [12, 36], it is very time-consuming to solve the convolution integrals during a dynamic analysis. Chen et al. [5, 6] replaced the convolution integral with a state-space model in modal coordinates. To make it more convenient to simulate the self-excited force in ABAQUS, this paper will model the time-history-dependent self-excited forces based on a state-space method in the Cartesian coordinate system. Because convolution is a linear operator, the integrals can be replaced by first-order differential equations

$$\dot{\mathbf{x}}_l = \dot{\mathbf{v}}(\mathrm{t}) - \frac{d_l V}{B}\mathbf{x}_l\ . \tag{10}$$

The following system of differential equations is obtained when all the state variables are considered

$$\dot{\mathbf{X}} = \begin{bmatrix} \dot{\mathbf{x}}_1 \\ \dot{\mathbf{x}}_2 \\ \vdots \\ \dot{\mathbf{x}}_{N-3} \end{bmatrix} = \frac{V}{B}\begin{bmatrix} -\mathbf{I}d_1 & & & \\ & -\mathbf{I}d_2 & & \\ & & \ddots & \\ & & & -\mathbf{I}d_{N-3} \end{bmatrix}\begin{bmatrix} \mathbf{x}_1 \\ \mathbf{x}_2 \\ \vdots \\ \mathbf{x}_{N-3} \end{bmatrix} + \begin{bmatrix} \mathbf{I} \\ \mathbf{I} \\ \vdots \\ \mathbf{I} \end{bmatrix}\dot{\mathbf{v}} = \mathbf{D}_c\mathbf{X} + \mathbf{E}_c\dot{\mathbf{v}}\ . \tag{11}$$

Here, **I** represents the identity matrix.

The equation of motion for the combined structure and flow system is obtained when Eqs. (9) and (11) are introduced into the equation of motion presented in Eq. (1)

$$\begin{cases} \mathbf{M}\ddot{\mathbf{v}}(\mathrm{t}) + (\mathbf{C} - \mathbf{A}_2)\dot{\mathbf{v}}(t) + (\mathbf{K} - \mathbf{A}_1)\mathbf{v}(t) - \mathbf{Z}(\mathrm{t}) = \mathbf{F}_{buff}(\mathrm{t}) \\ \dot{\mathbf{X}}(\mathrm{t}) = \mathbf{D}_c\mathbf{X}(\mathrm{t}) + \mathbf{E}_c\dot{\mathbf{v}}(\mathrm{t}) \\ \mathbf{Z}(\mathrm{t}) = \mathbf{Q}\mathbf{X}(\mathrm{t}) \end{cases} . \tag{12}$$

The time-history-dependent part of the self-excited forces, **Z(t)**, has been expressed in State-Space form. The velocity $\dot{\mathbf{v}}(\mathrm{t})$ and **Z(t)** are the input and output of the state-space model, respectively, and **X(t)** is the state variables. The state variables need to be included when solving for the dynamic equilibrium that governs the combined structure and flow system. Øiseth [12] introduced the state variables as additional aerodynamic degrees of freedom in the nodes of a beam element. Promising results were presented for a simple beam with similar properties to a long-span bridge. It is, however, a significant drawback that it is rather complicated to introduce additional degrees of freedom into existing finite element programs. It is also possible to solve the state variables directly without introducing them into the global finite element model. The displacement degrees of freedom of the finite element model and the state variables are in this paper solved separately for each time step. The starting point is the first-order linear inhomogeneous differential equation presented in Eq. (11). The differential equation can be solved by multiplying it by an integration factor, in our case $e^{-\mathbf{D}_c t}$, and integrating both sides to find **X** (see, for instance, [37] for further details)

$$e^{-\mathbf{D}_c t}(\dot{\mathbf{X}} - \mathbf{D}_c\mathbf{X}) = e^{-\mathbf{D}_c t}\mathbf{E}_c\dot{\mathbf{v}} . \tag{13}$$

The left-hand side of Eq. (13) is equal to the derivative of the product $e^{-\mathbf{D}_c t}\mathbf{X}$, so the equation may be written as follows

$$\frac{d(e^{-\mathbf{D}_c t}\mathbf{X})}{dt} = e^{-\mathbf{D}_c t}\mathbf{E}_c\dot{\mathbf{v}} . \tag{14}$$

The state variable **X** can be solved by integrating both sides of the equation from ($\mathbf{X}_k$,t_k) to ($\mathbf{X}_{k+1}$,t_{k+1})

$$\int_{(\mathbf{x}_k, t_k)}^{(\mathbf{x}_{k+1}, t_{k+1})} d(e^{-\mathbf{D}_c t}\mathbf{X}) = \int_{t_k}^{t_{k+1}} e^{-\mathbf{D}_c \tau}\mathbf{E}_c\dot{\mathbf{v}}(\tau)d\tau . \tag{15}$$

The solution depends on how the input $\dot{\mathbf{v}}(\tau)$ varies over the time step. A zero-order hold assumption where the input is assumed constant in the interval is often used

$$\dot{\mathbf{v}}(\tau) = \dot{\mathbf{v}}_k , \quad t_k \le \tau \le t_{k+1} . \tag{16}$$

In our case, it is essential to save as much computational effort as possible, and this makes a first-order hold assumption attractive, assuming that the input varies linearly over the time step. The dynamic response of the system can be obtained using Newmark's method [38], and because the velocity of the structure is used as input in the state-space model, it is natural to use the same approximation for the velocity as introduced in the Newmark time integration scheme

$$\dot{\mathbf{v}}(\tau) = \dot{\mathbf{v}}_k + [(1-\gamma)\ddot{\mathbf{v}}_k + \gamma\ddot{\mathbf{v}}_{k+1}](\tau - t_k), \quad t_k \le \tau \le t_{k+1}. \tag{17}$$

γ is a parameter in Newmark's method. The first-order hold assumption makes the implementation of the model slightly more complicated, but it will be demonstrated later that the first-order hold assumption is far better than the zero-order hold assumption in the sense that much larger time steps can be used in the numerical integration of the equation of motion. Inserting Eq. (17) into Eq. (15), assuming a constant time step Δt and performing the integration results in the following equation for the state variable at time t_{k+1}

$$\mathbf{X}_{k+1} = \mathbf{D}\mathbf{X}_k + \mathbf{E}\mathbf{v}_k + \mathbf{G}[(1-\gamma)\ddot{\mathbf{v}}_k + \gamma\ddot{\mathbf{v}}_{k+1}]. \tag{18}$$

Here, $\mathbf{D} = e^{\mathbf{D}_c\Delta t}$, $\mathbf{E} = (\mathbf{D}-\mathbf{I})\mathbf{D}_c^{-1}\mathbf{E}_c$, and $\mathbf{G} = \mathbf{D}_c^{-1}(\mathbf{E}-\mathbf{E}_c\Delta t)$. The exponential of matrix $\mathbf{D}_c\Delta t$, is the $n\times n$ matrix given by the power series $e^{\mathbf{D}_c\Delta t} = \sum_{k=0}^{\infty}\frac{1}{k!}(\mathbf{D}_c\Delta t)^k$. Here n is the dimension of matrix $\mathbf{D}_c\Delta t$. The corresponding equation for the zero-order hold case is obtained by setting $\mathbf{G} = 0$. Finally, the equation of motion in discrete form can be expressed as

$$\begin{cases} \mathbf{M}\ddot{\mathbf{v}}_k + (\mathbf{C}-\mathbf{A}_2)\dot{\mathbf{v}}_k + (\mathbf{K}-\mathbf{A}_1)\mathbf{v}_k - \mathbf{Z}_k = \mathbf{F}_{buff\_k} \\ \mathbf{X}_{k+1} = \mathbf{D}\mathbf{X}_k + \mathbf{E}\dot{\mathbf{v}}_k + \mathbf{G}[(1-\gamma)\ddot{\mathbf{v}}_k + \gamma\ddot{\mathbf{v}}_{k+1}] \\ \mathbf{Z}_k = \mathbf{Q}\mathbf{X}_k \end{cases}. \tag{19}$$

Compared to the normal equation of motion, Eq. (19) adds a new term, the output of the state-space model $\mathbf{Z}_k$. To check the performance of the framework, different time steps are used in the calculation of the self-excited force acting on per unit length of the girder in the vertical and torsional directions, as shown in Fig. 2. The wind velocity in this case is 40 m/s. Under the first-order hold assumption, the self-excited force has already converged when the time step is 0.2 s; meanwhile, for the zero-order hold case, the force does not converge until the time step decreases to 0.02 s. Therefore, a much larger time step can be used if the first-order hold is assumed, which can reduce the massive numerical effort.

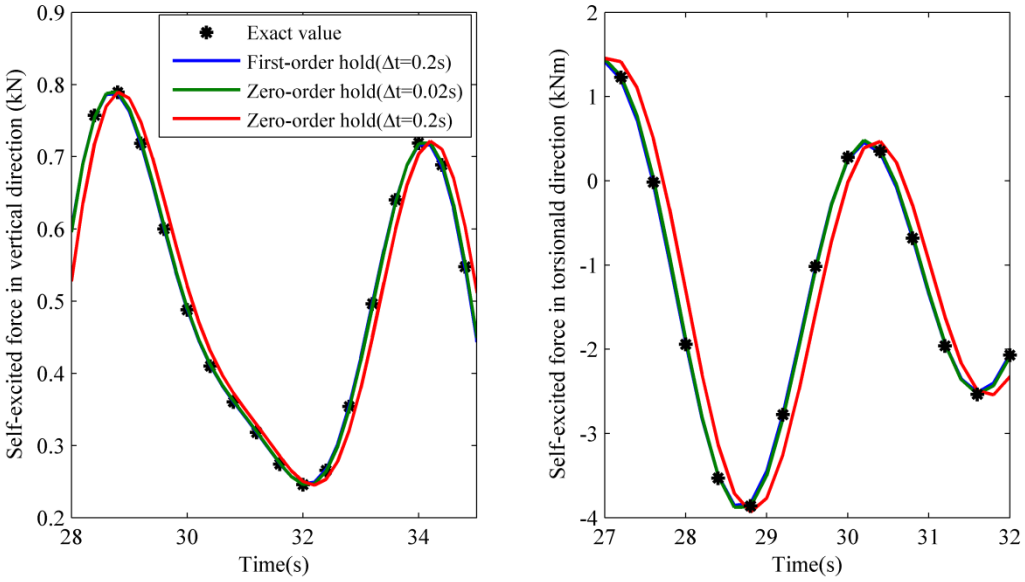

Fig. 2 Simulation of self-excited forces using different time steps

2.1.3 Implementation in ABAQUS

As shown in Eq. (19), the self-excited force in the time domain includes three terms: $\mathbf{A}_2\dot{\mathbf{v}}_k$ and $\mathbf{A}_1\mathbf{v}_k$, which are independent of the motion history, and the history-dependent term $\mathbf{Z}_k$, which is obtained from the state-space model replacing the convolution integrals. The history-dependent term is dependent on the state variables, structural velocity and acceleration in the previous time step and also the acceleration in the current time step if the first-order hold approximation is used. In ABAQUS, a user element is implemented to include the self-excited forces in the dynamic analysis. The element is developed as a one-node element, but it is also straightforward to implement it as a beam-type element. The elements are modelled on top of the nodes of ordinary beam elements such that it is not necessary to implement the mass, damping and stiffness terms related to the structure. The contribution to the residual force and its derivative or Jacobean matrix needs to be supplied in the user subroutine that defines the user element, as shown in *Algorithm* 1. The terms $\mathbf{A}_2\dot{\mathbf{v}}_k$ and $\mathbf{A}_1\mathbf{v}_k$ are easily implemented since $\mathbf{A}_1$ and $\mathbf{A}_2$ are constant. Because the state variable $\mathbf{X}_k$ is dependent on the acceleration in the same time step $\dot{\mathbf{v}}_k$, it is necessary to reorganize Eq. (18). This is accomplished by introducing the variable $\tilde{\mathbf{X}}_k = \mathbf{D}\mathbf{X}_{k-1} + \mathbf{E}\dot{\mathbf{v}}_{k-1} + \mathbf{G}(1-\gamma)\ddot{\mathbf{v}}_{k-1}$ such that the term $\mathbf{G}\gamma\ddot{\mathbf{v}}_k$ can be added directly into the mass matrix of the system. Meanwhile, $\tilde{\mathbf{X}}_k$ can be easily calculated using the already

known displacement, velocity, acceleration and state vector in the previous step ($\mathbf{v}_{k-1}$, $\dot{\mathbf{v}}_{k-1}$, $\ddot{\mathbf{v}}_{k-1}$ and $\mathbf{X}_{k-1}$).

To sum up, the presented approach uses state-space models to replace the convolution integrals in the representation of the self-excited forces in time domain, making the numerical simulation more efficient. A first-order hold assumption is applied in the approximation of the velocity over each time step, which makes the implementation of the state-space method more complicated but allows much larger time steps in the numerical simulation. By defining a user element, the state-space models are convenient to be implemented in ABAQUS.

Algorithm 1. Implementation of the user element in ABAQUS

Step (1): ABAQUS supplies current estimates of $\mathbf{v}_k$, $\dot{\mathbf{v}}_k$ and $\ddot{\mathbf{v}}_k$

Step (2): Load $\tilde{\mathbf{X}}_{k-1}$, $\dot{\mathbf{v}}_{k-1}$ and $\ddot{\mathbf{v}}_{k-1}$ from the last time step (the initial value of $\tilde{\mathbf{X}}: \tilde{\mathbf{X}}_0 = \mathbf{0}$) and

calculate the state vector $\mathbf{X}_{k-1}$

$$\mathbf{X}_{k-1} = \tilde{\mathbf{X}}_{k-1} + \mathbf{G}\gamma\ddot{\mathbf{v}}_{k-1}$$

Step (3): Calculate the residual force and Jacobian

$$\mathbf{R}_k = \mathbf{M}_{user}\ddot{\mathbf{v}}_k + \mathbf{C}_{user}\dot{\mathbf{v}}_k + \mathbf{K}_{user}\mathbf{v}_k + \mathbf{Q}\tilde{\mathbf{X}}_k$$

$$\mathbf{J} = \mathbf{M}_{user}\frac{1}{\beta\Delta t^2} + \mathbf{C}_{user}\frac{\gamma}{\beta\Delta t} + \mathbf{K}_{user}$$

where $\mathbf{M}_{user} = -\mathbf{QG}\gamma$, $\mathbf{C}_{user} = -\mathbf{A}_2$, and $\mathbf{K}_{user} = -\mathbf{A}_1$

$$\tilde{\mathbf{X}}_k = \mathbf{D}\mathbf{X}_{k-1} + \mathbf{E}\dot{\mathbf{v}}_{k-1} + \mathbf{G}(1-\gamma)\ddot{\mathbf{v}}_{k-1}$$

β and γ are the two parameters in Newmark's method

Step (4): Save $\tilde{\mathbf{X}}_k$, $\dot{\mathbf{v}}_k$ and $\ddot{\mathbf{v}}_k$ as solution-dependent variables and return to (1) for a new time step

or end.

2.2 Mean and buffeting forces

The mean and buffeting forces refer to the load due to the mean and fluctuating wind velocity, which can be calculated based on quasi-steady theory [39]. The effect of frequency-dependent aerodynamic admittance on the buffeting force is not considered in this paper. Moreover, only forces acting on the girder are considered.

3 Long-term extremes

It is possible to use short-term and long-term methods to calculate the characteristic values of extreme load effects due to wind for ULS design checks. In the short-term approach, the load effects are analyzed during a storm with an N-year-return period of a specified duration, e.g., 100 years and 10 min, while all storms during the long-term period are considered in the long-term approach. A short-term approach is necessary in practice from a computational point of view, but the extreme values obtained using the short-term approach need to be multiplied by a factor to obtain the characteristic values for the long-term period because less severe environmental conditions that occur more frequently and rare but more severe environmental conditions will contribute to the long-term extreme value distribution. This implies that the short-term approach needs to be verified using a full long-term approach.

3.1 Short-term statistics of extreme values by the ACER method

For a short-term process, the definition of the cumulative distribution function (CDF) of extremes η can be expressed as [28]

$$F_{\hat{P}(T)}(\eta) = \text{Prob}\{P_1 \le \eta, ..., P_N \le \eta\}. \tag{20}$$

Here, P_1, …, P_N refer to the observed values in the stationary short-term process (10 min), and $\hat{P}(T)$ is defined as the maximum value during the time interval T. The CDF of the extreme values can be obtained using a number of methods (see, for instance, [30, 31, 40]). The ACER method, developed by Naess and Gaidai, is applied in this paper because it is more flexible and less restrictive than methods based on asymptotic extreme value theory. The method introduces the concept of conditional exceedance probability, which is defined as

$$\alpha_{kj}(\eta) = \text{Prob}\{P_j > \eta \,|\, P_{j-1} \le \eta, ..., P_{j-k+1} \le \eta\}, \; 2 \le \text{k} \le \text{j} \le \text{N}. \tag{21}$$

Here, $\alpha_{kj}(\eta)$ is the exceedance probability conditional on k-1 previous non-exceedances of the threshold η, and N is the number of data observed in the process. Assuming that the conditional exceedances are a sequence of independently and identically distribution random variables following a Poisson process, the CDF of the extremes in Eq. (20) can be approximated by [28]

$$F_{\hat{P}(T)}(\eta) \approx \exp\left\{-\sum_{j=k}^{N} \alpha_{kj}(\eta)\right\}. \tag{22}$$

Here, $\sum_{j=k}^{N} \alpha_{kj}(\eta)$ is equal to the expected number of exceedances of the threshold η during the time interval T. In the numerical implementation it is convenient to introduce the concept of average conditional exceedance rates, defined as follows (see [28] for further details)

$$\varepsilon_k(\eta) = \frac{1}{N-k+1} \sum_{j=k}^{N} \alpha_{kj}(\eta), \quad k = 2,3,... << N, \;\; k \le j \le N. \tag{23}$$

Combining Eqs. (23) and (22), the CDF for the extreme value for the short-term process can be written as

$$F_{\hat{P}(T)}(\eta) \approx \exp\left\{-\varepsilon_k(\eta)\bar{N}T\right\}. \tag{24}$$

Here, $\bar{N}$ is the average number of observed values per unit of time. Naess and Gaidai [28] assumed that the mean exceedance rate $\varepsilon_k(\eta)$ in the tail of the distributions is dominated by a function of the form $q(\eta)\exp\left\{-e(\eta-b)^c\right\}(\eta \ge \eta_1 \ge \mathrm{b})$, where e, b and c are suitable constants. q is a function of the threshold, but its variation in the tail region is usually sufficiently slow compare with the exponential function [28] such that it can be taken as constant. Therefore, it's assumed to be replaced by a constant. η_1 is an appropriately chosen tail level. The four parameters e, b, c and q can be obtained by curve-fitting the expression to the data obtained from Eq. (23) utilizing the Levenberg-Marquardt least squares optimization method.

3.2 Long-term statistics of extreme values

The long-term process is not stationary, making the average conditional exceedance rates time-variant. Generalizing Eq. (24) to the non-stationary case, the corresponding expression of the CDF of extremes in the long-term case [41] is

$$F_{\hat{P}(T_L)}(\eta) = \exp\left\{-\int_0^{T_L} \varepsilon_k(\eta,t)\bar{N}\,\mathrm{d}t\right\}. \tag{25}$$

Here, T_L represents the long-term period. A long-term non-stationary stochastic process can be considered as a sequence of short-term stationary processes. Assuming that the stochastic process is ergodic, the integral in Eq. (25) can be expressed as

$$\int_0^{T_L} \varepsilon_k(\eta,t)\bar{N}\,\mathrm{d}t = T_L\bar{N}\int_{\mathbf{w}} \varepsilon_k(\eta\,|\,\mathbf{w})\,f_{\mathbf{w}}(\mathbf{w})\,\mathrm{d}\mathbf{w}\,. \tag{26}$$

Here, **w** represents parameters used to characterize the environmental loading, for instance, the mean wind velocity, while $f_{\mathbf{w}}(\mathbf{w})$ is the joint probability density distribution for the parameters. $\varepsilon_k(\eta\,|\,\mathbf{w})$ is the conditional ACER for the specific short-term period characterized by the environmental parameters **w**. See [41] for further details. Combining Eqs. (26) and (25), the CDF of the long-term extremes can be written as

$$F_{\hat{P}(T_L)}(\eta) = \exp\left\{-\bar{N}T_L\int_{\mathbf{w}} \varepsilon_k(\eta\,|\,\mathbf{w})\,f_{\mathbf{w}}(\mathbf{w})\,\mathrm{d}\mathbf{w}\right\},\quad T\to\infty\,. \tag{27}$$

4. Case study: The Hardanger Bridge

The Hardanger Bridge shown in Fig. 3 is used as a case study to verify the time-domain method introduced in this paper. The bridge has a main span of 1310 m and towers that are 186 m high. The distance between the two main cables is only 14.5 m, making it one of the slenderest bridges in the world. It crosses the Hardanger fjord between Vallavik and Bu in Norway. Tall mountains dominate the surrounding topography such that the mean wind direction is usually along the fjord and, hence, perpendicular to the bridge (see Fig. 4 for more details). The wind conditions were monitored at the site for five years before the bridge was designed. These records confirm that it is reasonable to assume that the strong winds are approaching the bridge perpendicular to the bridge deck. The probability distribution for the 10-minute mean wind velocity forms the basis of the long-term assessment of the extreme value distribution of the load effects. The Weibull distribution applied is shown in Fig. 5. A comprehensive finite element model of the bridge, displayed Fig. 6, is used in the dynamic analysis. To simulate the self-excited forces of the long and slender bridge in the dynamic analysis, an aerodynamic element is defined and implemented in ABAQUS. The element is developed as a one-node element that is included on the nodes along the bridge deck, as shown by the red markers in the figure.

Fig. 3 The Hardanger Bridge

Fig. 4 Map showing the shrouding topography

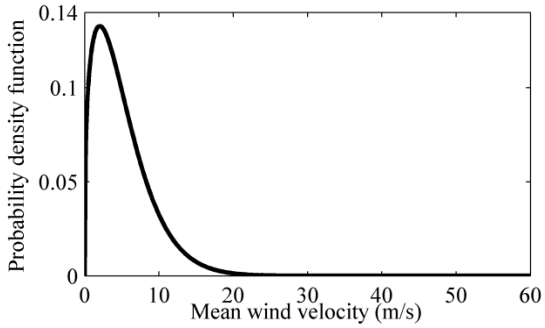

Fig. 5 Weibull distribution of the 10-minute mean wind velocity at the site

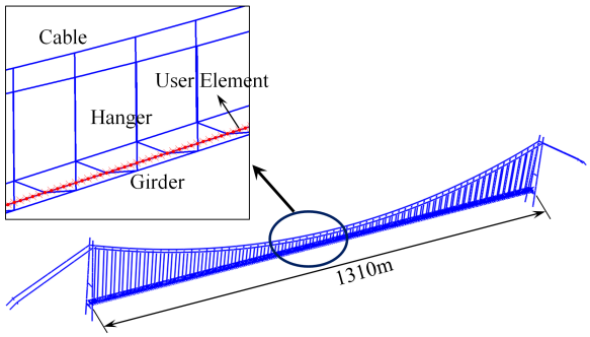

Fig. 6 Finite element model of the Hardanger Bridge

4.1 Curve fitting rational functions to the aerodynamic derivatives

Curve-fitting the expressions presented in Eq. (5) to the experimental data of the aerodynamic derivatives is the first step in time-domain wind-induced response analysis. The quality of the curve fit is of great importance for the accuracy of the numerical simulations because the self-excited forces need to be captured accurately in the entire reduced frequency ranges, especially the range corresponding to the natural frequencies of the system. Experimental results for the aerodynamic derivatives are commonly not available at high reduced velocities due to the restrictions of experimental conditions. Aerodynamic derivatives represented by rational function can commonly not converge to the value based on quasi-steady theory as the reduced velocity goes to infinity, as shown in the second and third column in Tab. 1. This is especially evident for P_1^*, which approaches a large positive value that will result in large negative damping at high reduced velocities. This limitation can, in some cases, cause numerical problems because it is the entire reduced frequency range that is considered in the inverse Fourier transform. In this paper, the quasi-steady theory for the self-excited forces is used to overcome this difficulty by assuming that the aerodynamic derivatives approach quasi-steady theory when the reduced frequency K goes to zero. This approach has also been used by

Salvatori and Borri [3]and Øiseth et al. [11]. As K goes to zero, the transfer function presented in Eq. (5) becomes

$$\lim_{K\to 0}\mathbf{F}(\omega)=\frac{1}{2}\rho V^2K^2[\hat{v}^2\mathbf{a}_1+\mathbf{i}\hat{v}(\mathbf{a}_2+\sum_{l=1}^{N-3}\frac{\mathbf{a}_{l+3}}{d_l})]\,.$$

The transfer function using quasi-steady theory reads [39]

$$\begin{aligned}\hat{\mathbf{F}}(\omega)&=i\omega\hat{\mathbf{C}}_{ae}(\omega)+\hat{\mathbf{K}}_{ae}(\omega)\\&=i\frac{\rho VB\omega}{2}\begin{bmatrix}-2(D/B)\bar{C}_D & \bar{C}_{\mathrm{L}}-(D/B)C'_D & 0\\ -2\bar{C}_{\mathrm{L}} & -\bar{C}_{\mathrm{L}}-(D/B)\bar{C}_D & 0\\ -2B\bar{C}_M & -BC'_M & 0\end{bmatrix}+\frac{\rho V^2B}{2}\begin{bmatrix}0 & 0 & (D/B)C'_D\\ 0 & 0 & C'_L\\ 0 & 0 & BC'_M\end{bmatrix}.\end{aligned}\tag{28}$$

Here, D and B are the height and width of the girder. $\bar{C}_D$, $\bar{C}_L$ and $\bar{C}_M$ are the mean values of the drag, lift and torsional moment force coefficients, and C'_D, C'_L and C'_M are their derivatives with respect to the attack angle. Introducing the assumption $\hat{\mathbf{F}}(\omega)=\lim_{K\to 0}\mathbf{F}(\omega)$, the matrices $\mathbf{a}_1$ and $\mathbf{a}_2$ can be expressed as follows

$$\mathbf{a}_1=\begin{bmatrix}0 & 0 & B(D/B)C'_D\\ 0 & 0 & BC'_L\\ 0 & 0 & B^2C'_M\end{bmatrix},\ \mathbf{a}_2=\begin{bmatrix}-2\bar{C}_D\,D\!\!\diagup\!\!B & \bar{C}_{\mathrm{L}}-C'_D\,D\!\!\diagup\!\!B & 0\\ -2\bar{C}_{\mathrm{L}} & -\bar{C}_{\mathrm{L}}-\bar{C}_D\,D\!\!\diagup\!\!B & 0\\ -2B\bar{C}_M & -BC'_M & 0\end{bmatrix}-\sum_{l=1}^{N-3}\frac{\mathbf{a}_{l+3}}{d_l}\,.\tag{29}$$

By substituting Eq. (29) into (5), only $\mathbf{a}_{l+3}$ and d_l are left as unknown variables. This simplifies the curve-fitting problem, but the d_l coefficients in the denominator still make the problem nonlinear. This implies that appropriate initial values for the (N-3)*10 unknowns have to be assumed, which can be a challenge. The curve-fitting problem is solved in two steps in this paper. The first step is to assume initial values for the d_l coefficients. The remaining coefficients are obtained using linear least squares. In the second step, the coefficients from step one are used as assumed initial values in a fully nonlinear curve-fitting problem where all the coefficients are considered. An optimal curve fit should not only match the data from the wind tunnel experiments but also approach the quasi-steady results as the reduced velocity goes to infinity. However, for several aerodynamic derivatives, it is challenging to satisfy both criteria. Take H_1^* and A_2^* as examples. As shown in Fig. 7, the curve fit for H_1^* satisfies both requirements, while that for A_2^* does not. The curve fit enforcing the quasi-steady asymptote is

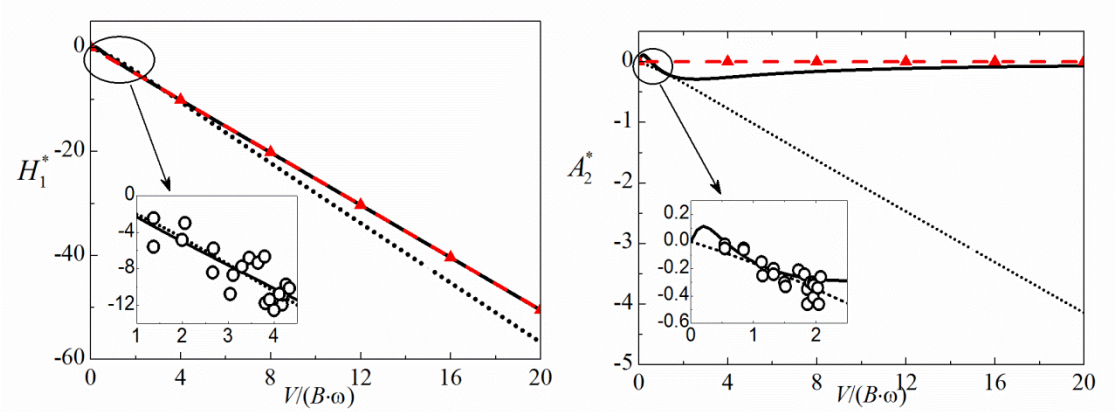

Fig. 7 Curve-fit of the aerodynamic derivatives H_1^* *and* A_2^* (—*Curve fit with quasi-steady asymptotes;* ••• *Curve fit without quasi-steady asymptotes;* -◢- *Quasi-steady asymptotes;* o *Experimental data*)

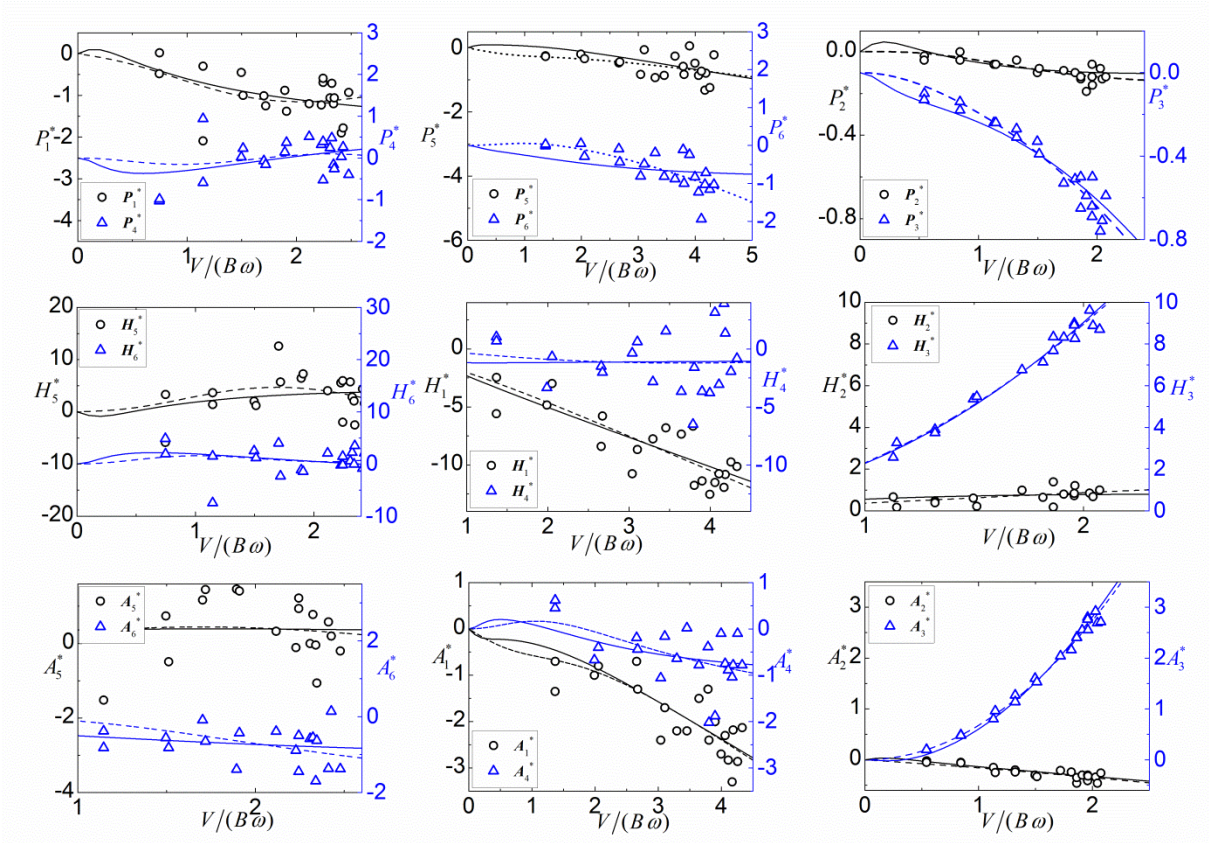

Fig. 8. Curve fit of the 18 aerodynamic derivatives. Solid lines are curve fits with quasi-steady asymptotes, while dashed lines are fits without.

inaccurate in the range of the experimental data. Because the dynamic response is very sensitive to inaccuracies in the reduced frequency range corresponding to the natural frequencies of the system, it is not recommended to enforce the quasi-steady asymptotes if it significantly reduces the accuracy of the fit.

The curve fits with and without quasi-steady asymptotes are shown in Fig. 8 using the coefficients, $\bar{C}_D$ =0.70, C'_D =0, $\bar{C}_L$ =-0.25, C'_L =2.4, $\bar{C}_M$ =0.01 and C'_M =0.74. Both curves fit the experimental data with fair accuracy. The largest discrepancy is P_6^*. However, the corresponding aerodynamic stiffness is very small compared to the structural stiffness. The discrepancy will thus not influence the response of the system significantly. The quasi-steady asymptotes for all the curve fits with quasi-steady limit are presented in the fourth column in Tab. 1. As the reduced velocity goes to infinity, all the aerodynamic derivatives, except KA_2^* and $K^2P_3^*$ which are not suggested to be enforced with quasi-steady limit, coincide with the quasi-steady results. The curve fits of aerodynamic derivatives both with and without quasi-steady asymptotes will be used in the flutter analysis to verify whether it is necessary to introduce the quasi-steady theory for curve fitting or not.

Tab.1 Comparison of quasi-steady asymptotes

	Quasi-steady Theory	Curve fit without Quasi-steady asymptotes	Curve fit with Quasi-steady asymptotes
Aerodynamic damping derivatives ($K\rightarrow 0$)			
KP_1^*	-0.2525	0.5153	-0.2525
KP_5^*	-0.25	-0.2086	-0.25
KP_2^*	0	0.0043	0
KH_5^*	0.5	-7.3223	0.5
KH_1^*	-2.53	-2.8489	-2.53
KH_2^*	0	0.4016	0
KA_5^*	-0.02	-0.4749	-0.02
KA_1^*	-0.74	-0.8099	-0.74
KA_2^*	0	-0.208	-0.178
Aerodynamic stiffness derivatives ($K\rightarrow 0$)			
$K^2P_4^*$	0	-0.2329	0
$K^2P_6^*$	0	-0.0592	0
$K^2P_3^*$	0	-0.1627	-0.1432
$K^2H_6^*$	0	2.2854	0
$K^2H_4^*$	0	0.0303	0
$K^2H_3^*$	2.4	2.2086	2.4
$K^2A_6^*$	0	0.0037	0
$K^2A_4^*$	0	-0.0086	0
$K^2A_3^*$	0.74	0.6994	0.74

4.2 Flutter analysis

It is recommended that a flutter analysis be conducted before performing time-domain simulations of the wind-induced dynamic response because it will be possible to verify that the system is stable and that the system has a reasonable amount of damping for the modes not covered by the experimental data of the aerodynamic derivatives. It can also be of interest to verify that the time-domain simulations capture the flutter vibrations at the correct mean wind speed because this confirms that the numerical framework introduced in this paper has converged with respect to the size of the time steps and the number of elements used in the simulations.

4.2.1 Multi-mode frequency-domain method

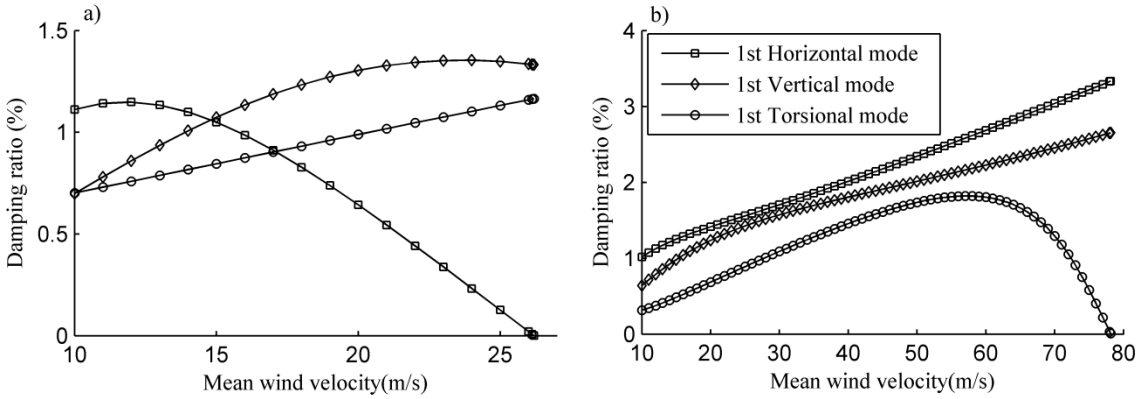

Fig. 9 Total damping for the 1st horizontal, vertical and torsional modes. a) use the curve fit of aerodynamic derivatives without quasi-steady asymptotes; b) with quasi-steady asymptotes

The multi-mode frequency-domain method is commonly used to calculate the critical velocity and frequency of a combined structure and flow system [1-3]. The critical velocity is defined as the mean wind velocity at which the damping ratio of one of the natural modes decreases to zero. Here, the first 20 still-air vibration modes are used as generalized coordinates to characterize the aero-elastic system. Fig. 9 shows the variation of the modal damping ratio for the 1st horizontal, vertical and torsional modes for increasing mean wind velocities. When using the curve fits without quasi-steady asymptotes, the damping ratio for the still–air horizontal mode decreases to zero rapidly due to the inappropriate curve fit of P_1^*, and the critical velocity is only 26.21 m/s. This corresponds to a reduced velocity of 4.55, which is clearly not within the range of the experimental data for the aerodynamic derivatives. The damping ratios when using the quasi-steady theory as asymptotes are displayed in Fig. 9(b). The damping ratios of the three modes increase with increasing mean wind velocity when V

is less than 60 m/s. This means that the wind-structure interaction generates positive modal damping for these modes. As the mean wind velocity continues to increase, the damping ratio for the 1st torsional mode starts to decrease, and it reaches zero when V is 78.16 m/s, which is recognized as the critical velocity.

4.2.2 Free vibration response

The critical velocity and corresponding frequency can also be obtained from the free vibration response of the combined structure and flow system. At low wind velocities, a decaying response will be observed, while an oscillation with constant or diverging amplitude will be observed when the system is unstable.

At the start of the time-domain simulation, an impulsive loading is imposed at the mid-span of the bridge. The free vibration response at the mid-span of the Hardanger Bridge under 40-, 78.3- and 80-m/s wind fields is displayed in Fig. 10. At 40 m/s, the system is clearly stable, while the response appears as undamped at 78.3 m/s, indicating that the system has zero damping. At 80 m/s, the response is clearly diverging. This corresponds very well to the results predicted using the multimode approach, which implies that both methods have converged and are able to accurately capture the self-excited forces in the system.

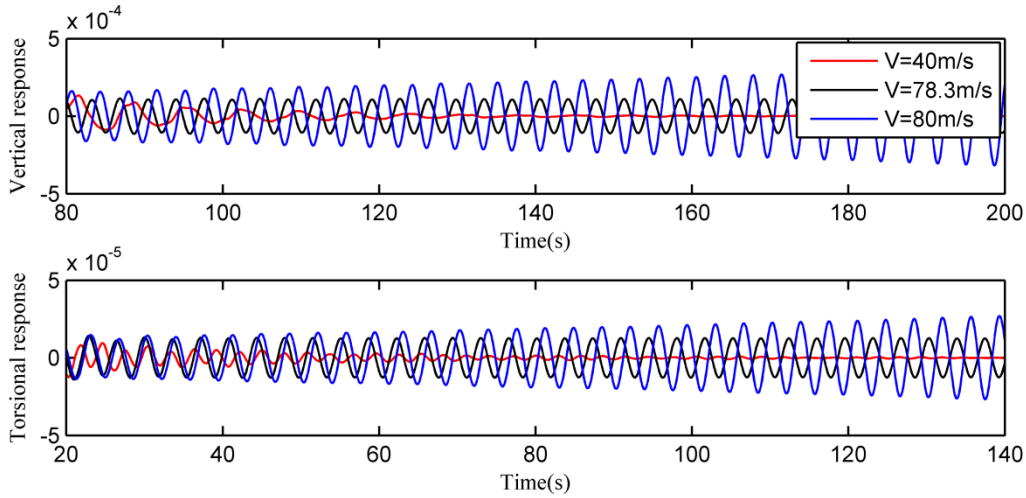

Fig. 10 Vertical and torsional responses at different wind velocities

4.3 Buffeting analysis

Time series of the wind-induced dynamic response are needed to obtain the long-term extreme value distributions of the load effects used in the design. The first step is to obtain the correlated time series of the fluctuating wind components, and the next step is to calculate the wind-induced dynamic response before the time series are processed to obtain the conditional mean exceedance rates needed in the long-term analysis.

4.3.1 Simulation of the wind field

The density of the air is assumed to be $\rho = 1.25\,\text{kg/m}^3$, and the co-spectral densities of the wind field are assumed to be given by

$$\begin{aligned} S_{uu}^{+}(\omega) &= \frac{40.58Vz\kappa}{(1+9.74\omega z/V)^{5/3}}\exp(-1.4\frac{\Delta x\omega}{V}) \\ S_{ww}^{+}(\omega) &= \frac{0.82Vz\kappa}{(1+0.79\omega z/V)^{5/3}}\exp(-\frac{\Delta x\omega}{V}) \\ S_{uw}^{+}(\omega) &= \frac{2.23Vz\kappa}{(1+1.67\omega z/V)^{7/3}}\exp(-\frac{\Delta x\omega}{V}) \end{aligned} \quad . \tag{30}$$

Here, *u* and *w* represent the horizontal along-wind and vertical components of the wind velocity; κ is the roughness coefficient at the site, assumed to be 0.0031; *z* is the height above the ground, and Δx is the distance between the two points considered. The fluctuating wind velocities have been simulated at 67 points along the girder through the use of Monte Carlo simulations, with a cut-off frequency of $\omega_u = 60$ rad/s and $\Delta\omega$=0.001 rad/s. See [12] for further details.

Time series of the two turbulence components at a mean velocity of 40 m/s are shown in Fig. 11. The average auto- and cross-spectral density of 20 realizations of the *u* and *w* components are compared with the target spectral densities in Fig. 12. As shown in the figure, the simulations seem to represent the target values very well.

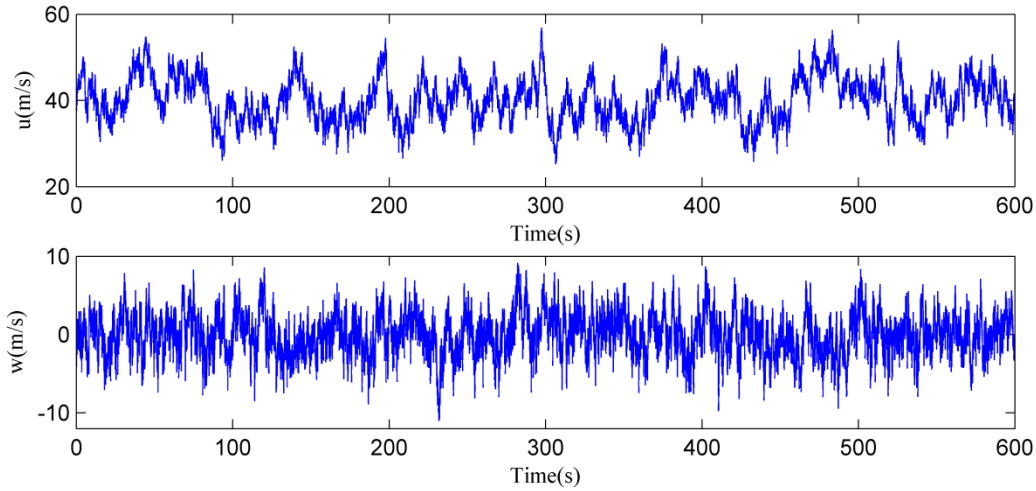

Fig. 11 wind velocities in the along-wind and vertical direction at the mid-span of the bridge. The mean wind velocity is 40 m/s

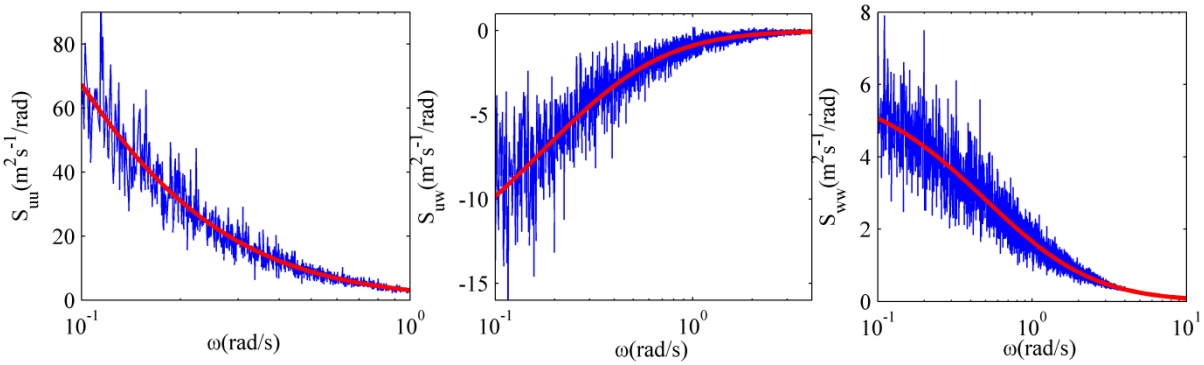

Fig. 12 Auto- and Cross-spectral density of the along wind and vertical wind velocities. (— Target spectrum density; — Average of 20 generated realizations)

4.3.2 Buffeting response for the linearized system

The time-domain methodology outlined in this paper should provide the same response as a multimode frequency-domain analysis if the system is linear. It is recommended that the time-domain simulations be verified by comparing their results with a frequency-domain analysis. This is important when experimental data of the aerodynamic derivatives are only available in a very limited reduced frequency range because the curves outside the range can cause unrealistic dynamic behavior. The wind-induced dynamic responses of the Hardanger Bridge at a mean wind velocity of 40 m/s are therefore calculated neglecting mean wind loads and nonlinear effects using the time- and frequency-domain approaches. The average auto- and cross-spectral densities for 10 time-domain simulations are compared to frequency-domain results in Fig. 13. The results correspond very well over the entire frequency range.

The variances obtained from the times series are also compared to frequency-domain results in Tab. 2. The discrepancy is large for several cases, for instance, cases 1 and 7 for the horizontal response and case 4 for the torsional response. However, the mean value corresponds very well for the horizontal and torsional responses (0.8% and 0.5% differences), and the difference is also small for the vertical response (3.79%). It is concluded that the time-domain simulations capture the dynamic behavior in an accurate manner.

4.3.3 Buffeting response considering nonlinearities

The bending moment about the horizontal axis along the girder and the axial force along the cable considering three mean wind velocities are presented in terms of the mean value and the mean value

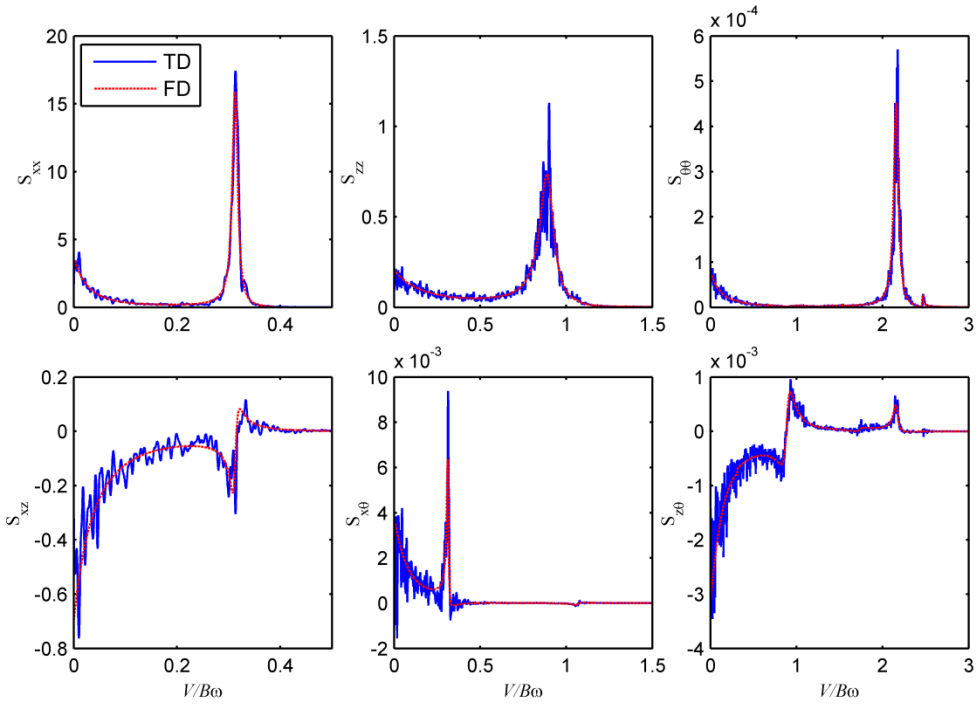

Fig. 13 Auto- and cross-spectral densities of the response at the mid-span of the bridge. V=40 m/s (TD and FD refer to time- and frequency-domain method; x,z and θ refer to the displacement in horizontal, vertical and torsional directions)

Tab. 2 Comparison of the variance of response from frequency- and time-domain simulations

	Horizontal Response (m)		Vertical Response (m)		Torsional Response ($\times 10^{-5}$ rad)	
	Multi-Mode Method					
	0.458		0.162		6.11	
	Time Domain Method					
Case 1	0.369	19.6 %	0.151	6.9 %	6.31	-3.3 %
Case 2	0.476	-3.9 %	0.147	9.2 %	6.23	-1.9 %
Case 3	0.439	4.1 %	0.155	4.6 %	5.72	6.3 %
Case 4	0.464	-1.2 %	0.157	3.1 %	7.61	-24.7 %
Case 5	0.467	-1.9 %	0.161	0.6 %	5.41	11.5 %
Case 6	0.453	1.1 %	0.156	4.0 %	5.40	11.6 %

Case 7	0.583	-27.1 %	0.164	-1.3 %	6.15	-0.7 %
Case 8	0.411	10.2 %	0.144	11.1 %	5.83	4.6 %
Case 9	0.424	7.4 %	0.164	-1.2 %	5.57	8.8 %
Case 10	0.458	0.1 %	0.161	0.9 %	6.56	-7.4 %
Mean Value	0.454	0.8 %	0.156	3.8 %	6.08	0.5 %

plus three standard deviations in Figs. 14 and 15. The axial force in the cable comes mainly from the self-weight of the bridge because the coefficient of variation is only approximately 4% for a wind velocity of 55 m/s. The maximum axial force occurs at the top of the towers as expected. For the section moment, the coefficient of variation is much larger. The mean value of the moment is mainly induced by the initial curvature of about 20000 m after installation and does not change significantly as the mean wind velocity increases. In addition, the variance of the bending moment is almost constant along the girder from 0.1 *L* to 0.9 *L*. Here *L* is the length of the girder.

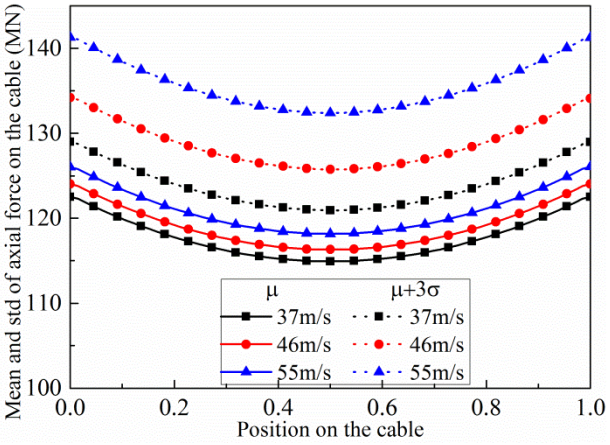

Fig. 14 Mean value and mean value plus three standard deviations of the axial force along the cable

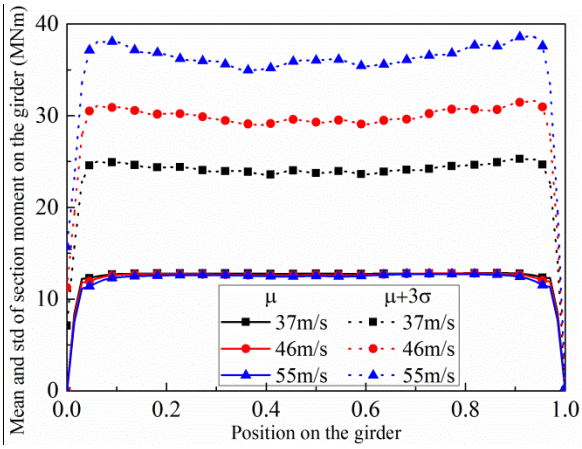

Fig. 15 Mean value and mean value plus three standard deviations of the moment along the girder

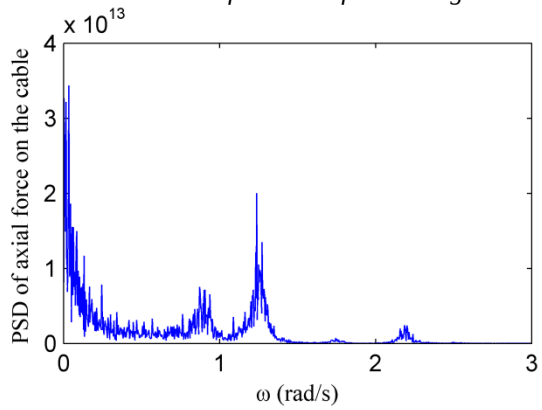

Fig. 16 Spectral density of the axial force in the cable at x=L and V=40 m/s

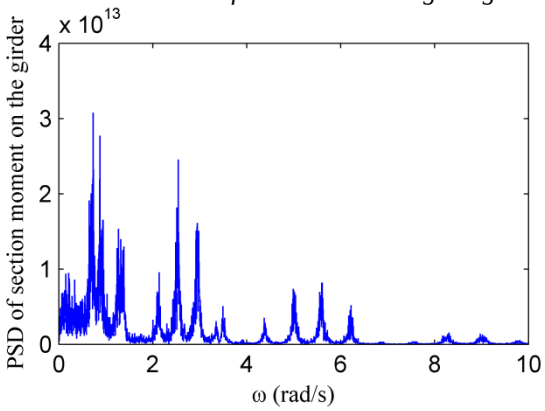

Fig. 17 Spectral density of the moment in the girder at x=0.1 L and V=40 m/s

The power spectral densities of the load effects are shown in Figs. 16 and 17. A background part and the first two peaks corresponding to the 2nd and 3rd vertical modes dominate the axial force in the cable. Several peaks dominate the spectral density of the bending moment in the girder. It is because

higher modes yield higher curvature, which provides high moments even if the response is small. It is important to take into account when selecting the spectral densities of the turbulence.

4.4 Extreme value analysis

The maximum axial force in the cable occurs at the towers, while the maximum bending moment in the girder is at $x = 0.1L$. These load effects are therefore considered in the long-term extreme value analysis. The drawback of the long-term approach is that it is not an economic choice from a computational point of view because the conditional average exceedance rates for all possible mean wind velocities are, in principle, required. It is, however, clear that it is only the mean wind velocities within a certain range that contribute to the long-term extreme value distribution. A simplified full long-term method and short-term method are used to estimate long-term extreme values and compare with the full long-term method.

4.4.1 Short-term extremes

The ACER method can be used to obtain the short-term distribution of the extreme value. The ACER functions of the bending moment considering different *k* values (2,100 and 200) are plotted in Fig. 18 at 42 m/s. This mean velocity corresponds to a return period of 100 years. Because the sampling rate is 12.5 Hz, *k*=200 corresponds to 16 seconds, which is larger than the natural period of all the modes. The ACER decreases as expected with increasing *k* values for low values of the bending moment because the upcrossings are not independent at this level. However, the data merges at large threshold values, which implies that the upcrossings for high levels are independent. The expression $\varepsilon_k(\eta) = q_k(\eta)\exp\left\{-e_k(\eta - b_k)^{c_k}\right\}$ is fitted to the data for *k*=2 in Fig. 19. The *p*-percentile extreme value can be obtained from Fig. 19 when

$$\varepsilon_2 \approx -\ln(F_{\hat{P}(T)}(\eta))/(\bar{N}T).$$

For example, 90% percentile of the extreme values corresponds to $\varepsilon_2 \approx 1.44\times10^{-5}$, which refers to a bending moment of 32.7 MNm, with 95% confidence intervals [31.4, 33.8] MNm. The contribution from this mean wind velocity to the long-term extremes distribution can be evaluated by inserting the ACER function into Eq. (27).

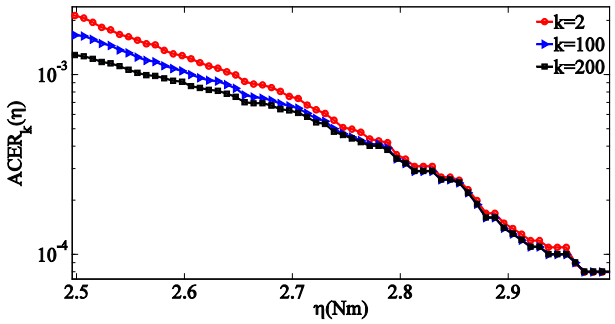

Fig. 18 ACER functions at different k values

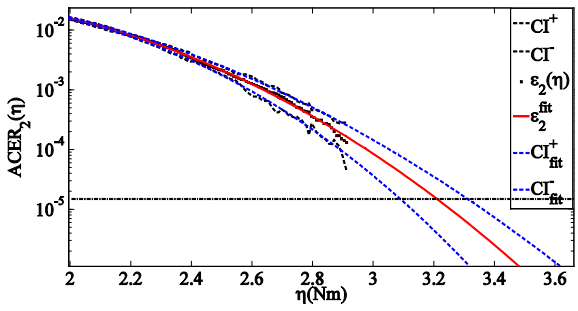

Fig. 19 Curve fit of the ACER function at k=2

4.4.2 Simplified full long-term extreme value analysis

To accurately calculate the long-term extremes of the load effects, the ACER functions for all possible mean wind velocities need to be obtained. It is therefore necessary to assess which mean wind velocities will yield significant contributions to the extreme value distribution of the load effects. The

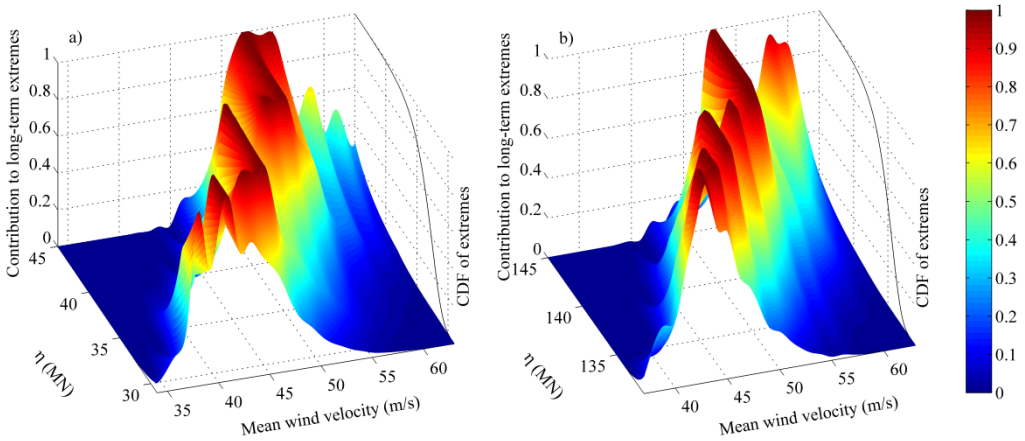

Fig. 20 Contribution from each wind velocity to the long-term extreme value distribution (a) Section moment on the girder; b) Axial Force on the cable)

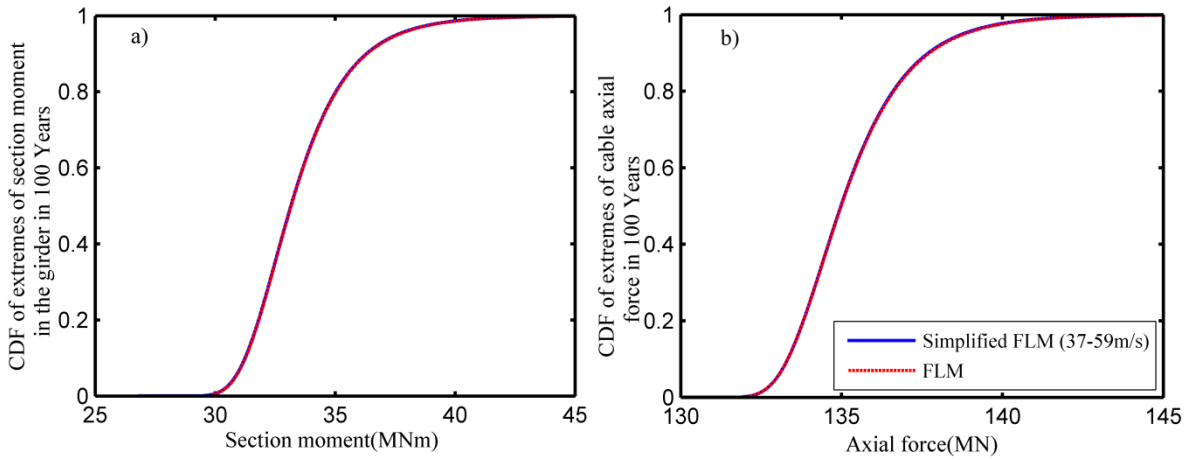

Fig. 21 Comparison of CDF of a) section moment in the girder and b) axial force in the cable based on full and simplified full long-term method

long-term extreme value distribution considering only the mean wind velocity can be written as

$$F_{\hat{P}(T_L)}(\eta) \approx \exp\left\{-\bar{N}T_L \sum_{i=1}^{N} \varepsilon_k(\eta \mid \mathrm{V}_i) f_v(\mathrm{V}_i)\Delta V\right\} \quad T \to \infty .$$

How much each mean wind velocity contributes to the extreme value distribution of the load effects is dependent on $\varepsilon_k(\eta \mid \mathrm{V}_i) f_v(\mathrm{V}_i)\Delta V$, which is the product of the conditional exceedance rates and the probability density of the corresponding mean wind velocity. By determining an appropriate range of wind velocities, tremendous unnecessary computational time can be avoided. The product of the up-crossing rate and the probability density function is plotted for a range of mean wind velocities in Fig. 20. The z-axis is $\frac{\varepsilon_k(\mathrm{V} \mid \eta) f_v(\mathrm{V})\Delta V}{Max(\varepsilon_k(\mathrm{V} \mid \eta) f_v(\mathrm{V})\Delta V)}$. When it gets closer to 1, the corresponding wind velocity is contributing more. If it approaches 0, the contribution to long-term extremes from this wind velocity can be ignored. As shown in the figure, it is only the mean wind velocities between 37 and 59 m/s that seem to yield significant contributions to the sum. The long-term extreme value distribution for the axial force in the cable and the bending moment in the girder are displayed in Fig. 21 based on the full long-term method (FLM) and simplified FLM. The figure confirms that it is only the velocity range between 37 and 59 m/s that contributes significantly. The most probable and 90% percentile of the long-term extreme bending moment are 32.53 and 36.33 MNm, respectively, while the results for the cable are 134.4 and 137.7 MN.

4.4.3 Comparison of short- and long-term extremes

It is very convenient to use short-term analysis of the dynamic response in the design of cable-supported bridges. However, the short-term approach cannot take into account the fact that the mean wind speeds that are slightly lower but occur more frequently and high mean wind speeds that occur rarely will contribute to the long-term extreme value distribution. Two approaches accounting for this effect in short-term analysis are applied in this case study and the results are presented in in Tab. 3 and 4.

In the first approach, one may select a higher percentile as the short-term characteristic instead of selecting the median extreme response. This approach has been popular for the wave load effects in offshore engineering. Regarding estimation of the 10^{-2}-annual probability value under wave actions, the 90% value is found to be a good estimate when the long-term variability is demonstrated by the

significant wave height and peak period [42]. However, only one varying characteristic (wind velocity) is involved in this paper. The best percentile selected to account for the short-term variability may be different from 90%. In short-term analysis, as shown in Tab. 3, if the median extreme is selected, the value is much smaller than the response value corresponding to 10^{-2}-annual exceedance probability in long-term analysis, which means that the corresponding 100-year response from the short-term method will be non-conservative. Through the comparison with long-term results, the 90%-percentile short-term extreme value of the section moment in the girder is very close to the long term response and recommended as the characteristic value for ULS design checks. Meanwhile, for the axial force on the cable, 92.5% percentile seems reasonable.

Another approach is to introduce a correction factor and multiply the median short-term extreme value by it. The short-term and long-term extreme values minus the axial force and bending moment due to gravity are shown in Tab. 4. The correction factor is approximately 1.133 and 1.145 for the bending moment on the girder and the axial force on the cable, respectively. The first approach has the advantage that it is not necessary to remove the mean value. However, the second approach is more applicable to this case since the variability of the correction factor in difference structural element is much smaller than the variability of the percentile.

Tab. 3 Extreme values of long- and short-term analysis

	Section moment on the girder (MNm)		Section force on the cable (MN)
Long-term extreme value (10^{-2}-annual probability value)	32.57	Long-term extreme value (10^{-2}-annual probability value)	134.47
Short term extreme value (Median)	30.28	Short term extremes (Median)	132.53
Short term extreme value (90%-percentile)	32.57	Short term extreme value (92.5%-percentile)	134.47

Tab. 4 Extreme values of long- and short-term analysis only consider the wind actions

	Section moment only due to wind actions (MNm)		Section force only due to wind actions (MN)
Short term extreme value (Median)	30.28-13=17.28	Short term extreme value (Median)	132.53-119.15=13.38
Long-term extreme value (10^{-2}-annual probability value)	32.57-13=19.57	Long-term extreme value (10^{-2}-annual probability value)	134.47-119.15=15.32
Correction factor γ	1.133	Correction factor γ	1.145

5. Conclusion

The time-domain prediction of long-term extreme value distributions of load effects for cable-supported bridges has been discussed in this paper.

The self-excited forces have been modeled using rational functions. Curve fitting the rational functions to the experimental data of the aerodynamic derivatives can be challenging, particularly if the experimental data are only available in a limited frequency range. It has been shown that these difficulties can be avoided if one assumes that the aerodynamic derivatives tend towards quasi-steady theory as the reduced velocity approaches infinity. If the quasi-steady limit is not enforced, the instability occurs in horizontal mode and the critical velocity is only 26.21 m/s, which is not physical for a reduced velocity not covered by experimental data. Meanwhile, the instability happens in torsional natural mode and the critical velocity increases to 78.16 m/s when quasi-steady limits are enforced in the curve fit of the rational function.

Efficient modelling of the self-excited forces is of crucial importance when using time-domain methods. It has been shown that one can model the history-dependent part of the self-excited forces using a discrete state-space model and that the state variables can be solved directly at the element level using either a first- or zero-order hold assumption. It has also been proved that significantly larger time steps can be used if the first-order hold assumption is used.

The critical velocity and buffeting response predicted considering a linearized finite element model has been calculated using the presented time-domain methodology and the traditional multimode approach. The results have been used to verify the time-domain methodology because the results in the time and frequency domains should be the same when the model is linear. The predicted critical velocities and the response spectra correspond very well.

Short-term and long-term predictions of characteristic load effects have been discussed. It has been found that the long-term extreme value distribution of the load effects can be obtained by applying the ACER method. It is concluded that the short-term extremes considering only wind loading should be multiplied by 1.2 to obtain the corresponding long-term extreme value for the quantile considered.

Acknowledgement

This research was conducted with financial support from the Norwegian Public Roads Administration. The authors gratefully acknowledge this support.

References

[1] Ge YJ, Tanaka H. Aerodynamic flutter analysis of cable-supported bridges by multi-mode and full-mode approaches. Journal of Wind Engineering and Industrial Aerodynamics. 2000;86:123-53.
[2] Katsuchi H, Jones NP, Scanlan RH, Akiyama H. Multi-mode flutter and buffeting analysis of the Akashi-Kaikyo bridge. Journal of Wind Engineering and Industrial Aerodynamics. 1998;77–78:431-41.
[3] Salvatori L, Borri C. Frequency- and time-domain methods for the numerical modeling of full-bridge aeroelasticity. Computers & Structures. 2007;85:675-87.
[4] Arena A, Lacarbonara W. Nonlinear parametric modeling of suspension bridges under aeroelastic forces: torsional divergence and flutter. Nonlinear Dynamics. 2012;70:2487-510.
[5] Chen X, Kareem A. Aeroelastic Analysis of Bridges under Multicorrelated Winds: Integrated State-Space Approach. Journal of Engineering Mechanics. 2001;127:1124-34.
[6] Chen X, Matsumoto M, Kareem A. Time Domain Flutter and Buffeting Response Analysis of Bridges. Journal of Engineering Mechanics. 2000;126:7-16.
[7] Costa C, Borri C. Application of indicial functions in bridge deck aeroelasticity. Journal of Wind Engineering and Industrial Aerodynamics. 2006;94:859-81.
[8] Diana G, Rocchi D, Argentini T, Muggiasca S. Aerodynamic instability of a bridge deck section model: Linear and nonlinear approach to force modeling. Journal of Wind Engineering and Industrial Aerodynamics. 2010;98:363-74.
[9] Lazzari M, Vitaliani RV, Saetta AV. Aeroelastic forces and dynamic response of long-span bridges. International Journal for Numerical Methods in Engineering. 2004;60:1011-48.
[10] Lin YY, Lieu YL. Geometrically nonlinear analysis of cable‐stayed bridges subject to wind excitations. Journal of the Chinese Institute of Engineers. 2003;26:503-11.
[11] Øiseth O, Rönnquist A, Sigbjörnsson R. Time domain modeling of self-excited aerodynamic forces for cable-supported bridges: A comparative study. Computers & Structures. 2011;89:1306-22.
[12] Øiseth O, Rönnquist A, Sigbjörnsson R. Finite element formulation of the self-excited forces for time-domain assessment of wind-induced dynamic response and flutter stability limit of cable-supported bridges. Finite Elements in Analysis and Design. 2012;50:173-83.
[13] Salvatori L, Spinelli P. Effects of structural nonlinearity and along-span wind coherence on suspension bridge aerodynamics: Some numerical simulation results. Journal of Wind Engineering and Industrial Aerodynamics. 2006;94:415-30.
[14] Zhang Z, Chen Z, Cai Y, Ge Y. Indicial Functions for Bridge Aeroelastic Forces and Time-Domain Flutter Analysis. Journal of Bridge Engineering. 2011;16:546-57.
[15] Caracoglia L, Jones N. Time domain vs. frequency domain characterization of aeroelastic forces for bridge deck sections. Journal of Wind Engineering and Industrial Aerodynamics. 2003;91:371-402.
[16] Scanlan RH, Tomko J. Air foil and bridge deck flutter derivatives. Journal of Soil Mechanics & Foundations Div. 1971.
[17] Scanolan R, Budlong K, Béliveau J. Indicial aerodynamic functions for bridge decks. Journal of Sanitary Engineering Division. 1974;100.
[18] Borri C, Costa C, Zahlten W. Non-stationary flow forces for the numerical simulation of aeroelastic instability of bridge decks. Computers & Structures. 2002;80:1071-9.
[19] K.L. R. Airplane math modelling methods for active control design. Structural Aspects of Control, AGARD Conference Proceeding. 1977;9:4.1-4.11.
[20] Arena A, Lacarbonara W, Valentine D, Marzocca P. Aeroelastic behavior of long-span suspension bridges under arbitrary wind profiles. Journal of Fluids and Structures. 2014;50:105-19.
[21] Agarwal P, Manuel L. Simulation of offshore wind turbine response for long-term extreme load prediction. Engineering Structures. 2009;31:2236-46.
[22] Krogstad HE. Height and period distributions of extreme waves. Applied Ocean Research. 1985;7:158-65.
[23] Naess A, Stansberg CT, Batsevych O. Prediction of Extreme Tether Tension for a TLP by the AUR and ACER Methods. Journal of Offshore Mechanics and Arctic Engineering. 2011;134:021103-.
[24] Sagrilo LVS, Naess A, Doria AS. On the long-term response of marine structures. Applied Ocean Research. 2011;33:208-14.

[25] Coles S, Bawa J, Trenner L, Dorazio P. An introduction to statistical modeling of extreme values: Springer; 2001.
[26] Gumbel EJ. Statistics of extremes: Courier Corporation; 2012.
[27] Cheng P, van Bussel G, van Kuik G, Vugts J. Reliability‐based Design Methods to Determine the Extreme Response Distribution of Offshore Wind Turbines. Wind Energy. 2003;6:1-22.
[28] Naess A, Gaidai O. Estimation of extreme values from sampled time series. Structural Safety. 2009;31:325-34.
[29] Ding J, Chen X. Assessment of methods for extreme value analysis of non-Gaussian wind effects with short-term time history samples. Engineering Structures. 2014;80:75-88.
[30] Holmes JD, Moriarty WW. Application of the generalized Pareto distribution to extreme value analysis in wind engineering. Journal of Wind Engineering and Industrial Aerodynamics. 1999;83:1-10.
[31] Simiu E, Heckert N. Extreme Wind Distribution Tails: A “Peaks over Threshold” Approach. Journal of Structural Engineering. 1996;122:539-47.
[32] Haver S, Kleiven G. Environmental Contour Lines for Design Purposes: Why and When? ASME 2004 23rd International Conference on Offshore Mechanics and Arctic Engineering: American Society of Mechanical Engineers; 2004. p. 337-45.
[33] Winterstein SR, Ude TC, Cornell CA, Bjerager P, Haver S. Environmental parameters for extreme response: Inverse FORM with omission factors. Proc 6th Int Conf on Structural Safety and Reliability, Innsbruck, Austria1993.
[34] Chen X. Extreme Value Distribution and Peak Factor of Crosswind Response of Flexible Structures with Nonlinear Aeroelastic Effect. Journal of Structural Engineering. 2014;140:04014091.
[35] Huang G, Chen X, Li M, Peng L. Extreme value of wind-excited response considering influence of bandwidth. Journal of Modern Transportation. 2013;21:125-34.
[36] Taghipour R, Perez T, Moan T. Hybrid frequency–time domain models for dynamic response analysis of marine structures. Ocean Engineering. 2008;35:685-705.
[37] D. S. Matrices: Theory and Applications. 2002.
[38] K. S. Non-linear Modeling and Analysis of Solids and Structure. Cambridge (New York). 2009.
[39] Strømmen E. Theory of bridge aerodynamics. 2010.
[40] Naess A, Gaidai O. Monte Carlo Methods for Estimating the Extreme Response of Dynamical Systems. Journal of Engineering Mechanics. 2008;134:628-36.
[41] Naess A. Technical note: on the long-term statistics of extremes. Applied Ocean Research. 1984;6:227-8.
[42] Naess A, Moan T. Stochastic dynamics of marine structures. 2012.